Sidelobe Suppression with Low Peak-to-Valley Power Ratio Waveforms in MIMO-OFDM Dual-Function Radar-Communication Systems

Xiang Feng, *Member, IEEE,* Zhongqing Zhao, *Student Member, IEEE,* Huiping Huang, *Member, IEEE,* Linlong Wu, *Senior Member, IEEE,* Zhanfeng Zhao, *Member, IEEE*

***Abstract*—In orthogonal frequency division multiplexing (OFDM)-based dual-function radar-communication (DFRC) systems, achieving low peak-to-average power ratio (PAPR) is essential for transmission efficiency and performance. Traditional PAPR constraints, however, fall short in managing the dynamic range of waveforms, thereby limiting power maximization. This study introduces a peak-to-valley power ratio (PVPR) constraint for multiple-input multiple-output (MIMO) DFRC systems to enhance hardware compatibility, waveform fidelity, and consistent transmission power. We develop low-PVPR OFDM waveforms tailored for MIMO-DFRC systems, improving both radar and communication functions. For radar applications, we optimize the weighted peak or integrated sidelobe level (WPISL) and employ phase-encoded waveforms to minimize sidelobes. For communication purposes, we implement a constructive interference (CI) design coupled with a waveform similarity error (WSE) constraint. Utilizing the majorization-minimization (MM) framework, we convert the non-convex problem into a series of convex ones. Numerical results demonstrate significant improvements in sidelobe reduction, symbol error rate (SER), and average achievable rate, thereby validating the effectiveness of our approach in enhancing DFRC systems.**

***Index Terms*—Dual-functional radar-communication (DFRC), waveform design, peak-to-valley power ratio, constructive interference, range sidelobe suppression.**

I. Introduction

In recent years, the dual-functional radar communication (DFRC) system utilizing multiple-input multiple-output (MIMO) technology has garnered significant attention [1]–[5]. Radar and communication signals usually share several common waveform characteristics. Although their primary purposes differ, it is feasible to repurpose one type of signal to perform the function of the other [3]. However, implementing radar signals for communication and vice versa introduces several challenges [6], [7]. These challenges would encompass managing signal interference, optimizing the balance between radar and communication performance, and ensuring reliable data exchange in dynamic environments.

A. Related Works

To tackle these challenges, spatial beamforming using multi-antennas, which leverages spatial degrees of freedom, has proven to be an effective method for implementing DFRC systems [8]–[21]. Various optimization-based transmit beamforming approaches have been explored for DFRC systems with both separate and shared antenna configurations [8]–[10], utilizing communication signals for target detection. For simultaneous radar target probing and multi-user (MU) communication, the DFRC transmitter must jointly precoded individual communication and radar waveforms. In [11], both communication and dedicated radar signals were employed to enhance the sensing performance. The work in [12] discussed a Pareto optimization framework for DFRC systems, aiming to optimize the trade-off between radar and communication performance through beamforming design, focusing on single-antenna communication users (CUs). Additionally, [13] designed a dual-functional base station (BS) to serve multi-antenna CUs and detect targets simultaneously using a hybrid analog/digital beamforming technique. Based on mutual information theory, [14] proposed an optimal spatio-temporal power mask design idea, and presented a typical packet-based signal structure, including training symbols. However, these studies mainly focused on beamforming and overlooked the waveform properties of each radar transmitter. Consequently, achieving beam direction matching through waveform design has gained considerable attention. For instance, [18] proposed a generalized framework considering worst-case scenarios where the steering vector does not match, using peak sidelobe level (PSL) or integrated sidelobe level (ISL) as objective functions. In [19], a low-complexity discrete Fourier transform (DFT)-based closed-form covariance matrix design technique was introduced to derive a novel solution for directly designing constant modulus waveforms and the desired beam. Recently, the symbol-level beamforming (SLB) technology based on constructive interference (CI) has attracted significant attention. This approach transforms multi-user interference (MUI)

Manuscript received xxxx. Corresponding author: Xiang Feng, Huiping Huang.

Xiang Feng, Zhongqing Zhao and Zhanfeng Zhao are with the School of information science and engineering, Harbin institute of technology, Weihai, 264209, China (E-mail: fengxiang@hit.edu.cn, 22S130416@stu.hit.edu.cn, zhaozhanfeng@hit.edu.cn). Their work was supported in part by Major Scientific and Technological Innovation Projects of Shandong Province of China (Grants 2021ZLGX05 and 2022ZLGX04), and the National Natural Science Foundation of China, Grant 42127804.

Huiping Huang is with Department of Electrical Engineering, Chalmers University of Technology, 41296 Gothenburg, Sweden (E-mail: huiping@chalmers.se).

Linlong Wu is with the Interdisciplinary Centre for Security, Reliability and Trust (SnT), University of Luxembourg, L-1855, Luxembourg (E-mail: linlong.wu@uni.lu). L. Wu's work was supported by the FNR CORE INTER project C20/IS/14799710/SENCOM.

into some meaningful signals, thereby enhancing communication quality of service (QoS) and offering greater design flexibility [20]. For example, [21] focused on SLB in large-scale MIMO systems with low-precision digital-to-analog converters (DACs), demonstrating a notable improvement in communication QoS compared to traditional methods.

Most of the aforementioned methods for DFRC systems focus on single carrier-frequency signals. It is important to note that orthogonal frequency division multiplexing (OFDM) signals are robust against multipath fading and offer high spectral efficiency [22]. In [22], the authors studied power allocation with a word error probability (WEP) constraint in OFDM-based DFRC systems. Similarly, [23] proposed a novel quadrature amplitude modulation (QAM), which utilizes sidelobe control and waveform diversity to transmit communication information. In their approach, downlink communication data is modulated by nulling the ambiguity function (AF) sidelobes within specific range-Doppler cells, while suppressing sidelobes around the AF mainlobe to maintain radar detection performance. In [24], the authors developed an objective function to measure the depth of AF nulling as a performance metric, focusing on the worst-case sidelobe level ratio across the targeted range-Doppler cells. It is known that joint radar-communication signals often have poor range sidelobes, making them less suitable for radar functions. To address this issue, [25] proposed a joint radar-communications approach that operates in pulsed radar mode. In this method, digital communication sequences are divided into blocks and mapped to digital phase-coded sequences, such as binary phase-shift keying (BPSK) and quadrature phase-shift keying (QPSK) sequences. To minimize the downlink multiuser interference, [26] discussed omnidirectional and directional beampattern design problems, considering weighted optimizations that allow for a flexible trade-off between radar and communication performance. Additionally, they introduced low-complexity algorithms to address the practical challenge of constant modulus waveform design. From a practical application perspective, to avoid nonlinear distortion of waveforms, common energy constraints such as constant modulus (CM) and low peak-to-average power ratio (PAPR) are imposed on the design of transmitted waveforms. However, the constant modulus constraint is often overly stringent and lacks flexibility, which can be detrimental to system performance [27], [28]. Similarly, the PAPR constraint does not sufficiently control the amplitude fluctuations of signal [29]. OFDM signal in wireless communication also faces these issues [30]. In the realm of waveform optimization and design, managing peak-to-valley variations in power is crucial to mitigate nonlinear distortions of transmission systems. The peak-to-valley power ratio (PVPR) constraint [31], or the dynamic range ratio (DRR) as referred to in [32], [33], emerges as a promising alternative. By focusing on the ratio between the peak and minimum (valley) power levels within the waveform, the PVPR/DRR constraint offers a more comprehensive approach to control amplitude variations, thereby reducing the likelihood of nonlinear distortions. This constraint provides some greater flexibility compared to the CM case, allowing for a wider range of waveform designs while still maintaining some tight control over power fluctuations.

B. Our Contributions

To address the limitations of current state-of-the-art methods, we focus on an OFDM-based DFRC system comprising a multi-antenna base station (BS) and multiple single-antenna user equipment (UEs). Designing low PAPR waveforms is essential for enhancing transmission efficiency and overall performance. However, some existing literature indicates that PAPR constraints alone may not adequately control the dynamic range of waveforms and can be detrimental to maximizing transmission power. Therefore, to better adapt to real hardware conditions, enhance waveform fidelity, and maintain uniform transmission power, we propose a waveform energy constraint based on the PVPR constraint. This constraint directly controls the dynamic distortion of waveform amplitude. We try to design low-PVPR DFRC MIMO-OFDM waveforms to achieve these goals. The main contributions of this paper are summarized as follows:

- For the radar functionality, we introduce an optimized weighted peak or integrated sidelobe level (WPISL) method and design phase-encoded waveforms to achieve local sidelobe reduction.
- For the communication functionality, we adopt a waveform design method based on CI, including waveform similarity error (WSE) constraint and a joint objective function for radar and communication.
- To address this challenging optimization problem, we employ the majorization-minimization (MM) framework and introduce auxiliary variables to transform the nonconvex problem into a series of convex ones, which is then solved by convex optimization techniques.
- Numerical results demonstrate that our approach surpasses current widely-used algorithms in reducing sidelobes. Additionally, the proposed CI-based approach outperforms existing least squares (LS) methods in terms of symbol error rate (SER) and average achievable rate.

The remaining sections of this paper are organized as follows. Section II describes the radar model and communication model, and introduces the waveform design problem. In Section III, a method based on the MM framework, incorporating auxiliary variables, is proposed to address the waveform design problem. Section IV validates the effectiveness of the proposed algorithm through simulation. Finally, in Section V, we summarize this article.

Notations: Unless otherwise specified, uppercase bold symbols represent matrices, while lowercase bold symbols represent vectors. The operators $(\cdot)^{\mathrm{T}}$, $(\cdot)^{\mathrm{H}}$, and $(\cdot)^{*}$ denote the transpose, the conjugate transpose, and the conjugate, respectively. The set of $N \times N$ complex matrices is denoted by $\mathbb{C}^{N\times N}$, and the set of n-dimensional complex vectors is denoted by $\mathbb{C}^{n}$, and j denotes the imaginary unit. The ℓ_2-norm is represented by $||\cdot||_2$, the ℓ_p-norm by $||\cdot||_p$, and the Frobenius norm by $||\cdot||_{\mathrm{F}}$. The notation $[\mathbf{X}]_{i,j}$ refers to the (i,j)th element of the matrix $\mathbf{X}$, and $\lambda_{\max}(\mathbf{X})$ denotes the maximum eigenvalue of the matrix $\mathbf{X}$. The symbols $\succeq$ (and $\succ$ for strictness) are used to denote positive semidefiniteness (and positive definiteness,

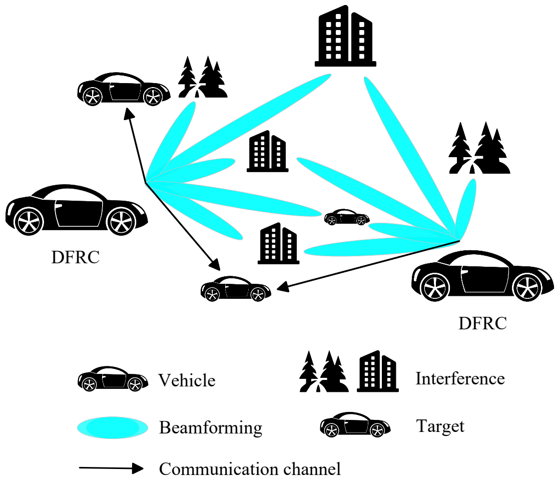

Fig. 1. A dual-functional radar communication system.

respectively) of matrices. The identity matrix of size $N \times N$ is denoted by $\mathbf{I}_N$. The operators $\mathrm{Re}(x)$ and $\mathrm{Im}(x)$ represent the real and imaginary parts of x, respectively. The notation $\mathrm{vec}(\cdot)$ denotes the matrix vectorization operator, $\mathrm{Tr}(\cdot)$ denotes the trace of a matrix, $\otimes$ represents the Kronecker product, and $\mathrm{diag}(\cdot)$ denotes the diagonal operator, which forms a diagonal matrix from its argument.

II. System Model

We consider a broadband MIMO-DFRC system for multiple vehicular users, as shown in Fig. 1, employing an integrated waveform for both detection and communication performance. Through the collaborative utilization and sharing of DFRC as a unified platform for radar and communication, this not only enhances the perceptual capabilities of vehicle but also enables more flexible and efficient communication. This system is equipped with N_t transmitting elements arranged in a uniform linear array (ULA) with element space d, whose primary objective is to serve K downstream single-antenna UEs while simultaneously sensing M distant targets.

A. OFDM-Based DFRC Waveforms

To enhance the performance of OFDM and mitigate the effects of inter-symbol interference (ISI) induced by multipath channels, this study adopts the conventional OFDM technology augmented with a cyclic prefix (CP) [34]. To facilitate theoretical analysis, we make the assumption that the CP length is not less than the maximum delay of the channel. For optimal synchronization and theoretical feasibility, the starting point of the DFT window for OFDM symbols is precisely determined within its guard interval. The base station achieves impeccable synchronization with radar pulses, enabling it to accurately discern the start and end times of radar pulses. The CP extends the OFDM symbol by appending a duplicate of its latter portion to the front. If the length of the CP exceeds or equals the maximum delay of the multipath signal, the ISI impact of an OFDM symbol on the subsequent one is confined within the guard interval. This ensures that the subsequent DFT transformation of the next OFDM symbol remains unaffected by ISI, with its period denoted as N_s. Let N_c represent the CP length in terms of the number of samples. Consequently, the resultant period of the extended OFDM symbol becomes $N = N_s + N_c$.

We first define $\mathbf{S} \in \mathbb{C}^{N_s K \times L}$ as the symbol data matrix for all UEs on N_s subcarriers, transmitted during a communication frame of length L. Additionally, $\mathbf{Q} = \mathrm{diag}(\mathbf{Q}_1, \ldots, \mathbf{Q}_{N_s}) \in \mathbb{C}^{N_s N_t \times N_s K}$ is the compact pre-coding matrix for all UEs on all subcarriers. Here, $\mathbf{Q}_n \in \mathbb{C}^{N_t \times K}$ represents the pre-coding matrix for all UEs on subcarrier. The transmit symbol data $\mathbf{S}$ is initially pre-encoded in the frequency domain by the matrix $\mathbf{Q}$. Before undergoing subcarrier modulation, the signal goes through an inverse discrete fourier transform (IDFT) operation to transform it into the time domain. Subsequently, we proceed to employ

$$\mathbf{X}_{\mathrm{s}} = \mathbf{QS} = \left[\mathbf{X}_1^{\mathrm{T}}, \cdots, \mathbf{X}_{N_s}^{\mathrm{T}}\right]^{\mathrm{T}} \in \mathbb{C}^{N_s N_t \times L}. \tag{1}$$

Prior to IDFT processing, the baseband pre-encoded symbol matrix across all subcarriers can be rewritten as $\mathbf{X}_n = [\mathbf{x}_1, \mathbf{x}_2, \ldots, \mathbf{x}_L] \in \mathbb{C}^{N_t \times L}$, and $\mathbf{x}_l$ is the N_t-dimensional spatial domain transmitting data at the lth moment. The normalized DFT matrix for data transmission is denoted as $\mathbf{F}_{\mathrm{DFT}} \in \mathbb{C}^{N_s \times N_s}$, where the (n,m)th element of $\mathbf{F}_{\mathrm{DFT}}$ is given as $\frac{1}{\sqrt{N_s}} e^{-\frac{j2\pi}{N_s}(n-1)(m-1)}$. Taking into account that the ULA is equipped with N_t transmitting antennas, the IDFT processing at the DFRC-BS transmitter is represented by the operation $\left(\mathbf{F}_{\mathrm{DFT}}^{\mathrm{H}} \otimes \mathbf{I}_{N_t}\right) \in \mathbb{C}^{N_s N_t \times N_s N_t}$. Consequently, the time-domain waveform after IDFT can be further represented as

$$\mathbf{G} = \left(\mathbf{F}_{\mathrm{DFT}}^{\mathrm{H}} \otimes \mathbf{I}_{N_t}\right) \mathbf{X}_{\mathrm{s}} \in \mathbb{C}^{N_s N_t \times L}. \tag{2}$$

For CP-based DFRC MIMO-OFDM waveforms, it is crucial to mitigate ISI caused by multipath frequency-selective fading, with the last N_c symbols repeating at the beginning of the original symbol sequence [35]. The DFT matrix is denoted as $\mathbf{F}_{\mathrm{c}}$, and the DFT matrix with CP is expressed as [36]

$$\mathbf{F} = [\mathbf{F}_{\mathrm{c}}, \mathbf{F}_{\mathrm{DFT}}] \in \mathbb{C}^{N_s \times N}. \tag{3}$$

Typically, the DFRC MIMO-OFDM waveform after the addition of CP can be represented as [37]

$$\dot{\mathbf{G}} \triangleq \left(\mathbf{F}^{\mathrm{H}} \otimes \mathbf{I}_{N_t}\right) \mathbf{X}_{\mathrm{s}} \in \mathbb{C}^{N N_t \times L}. \tag{4}$$

Following the above discussion, the receiver can exploit the orthogonality of subcarriers for signal demodulation. This is achieved by performing IDFT at the transmitter, adding the CP, and subsequently removing the CP and applying DFT at the receiver. The signal processing flow in an OFDM-based DFRC system is succinctly illustrated in Fig. 2. Fig. 2 depicts the complete signal processing chain of the DFRC system. It includes the data symbols being modulated using PSK, followed by waveform optimization, IDFT, and the addition of a CP before transmission. At the receiver end, the CP is removed, and a DFT is applied to recover the transmitted signal. This sequence effectively mitigates the impact of frequency-selective fading-induced ISI and ensures accurate demodulation and radar processing [34].

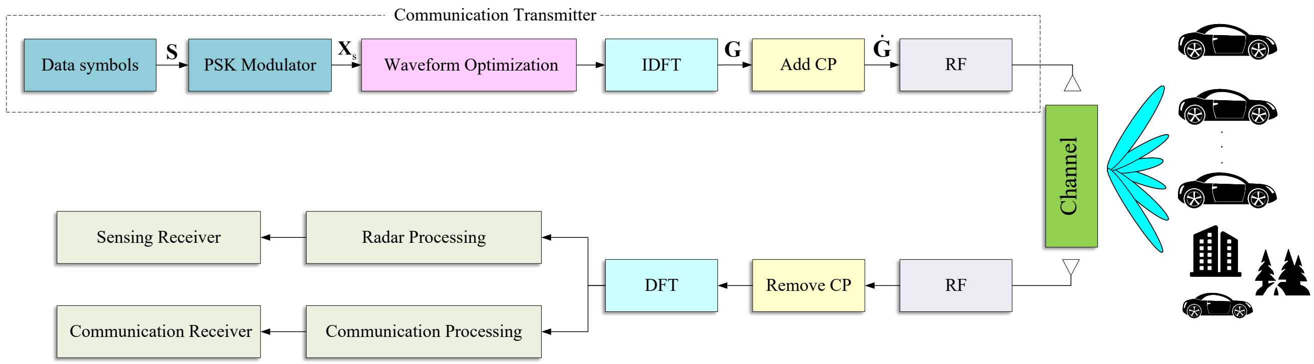

Fig. 2. Signal processing block scheme in MIMO-DFRC system

B. Constructive interference for Communications

The signal incorporated with CP should undergo modulation onto subcarriers and then be converted into the radio frequency (RF) domain. Subsequently, it is transmitted through N_t RF chains connected to N_t antennas. The communication channel extending from the DFRC-BS to the downstream UEs in the link is presumed to manifest as a broadband frequency-selective fading channel. This presumption remains valid given the condition of time invariance over a sufficiently extended time scale [26]. The received signal for the symbol-data sequence can be expressed as

$$\mathbf{Y}_{\rm s} = \underbrace{\mathbf{S}}_{\text{Signal}} + \underbrace{(\mathbf{H}_{\rm s}\mathbf{X}_{\rm s} - \mathbf{S})}_{\text{MUI}} + \underbrace{\mathbf{W}_{\rm s}}_{\text{Noise}}, \tag{5}$$

where $\mathbf{W}_{\rm s}$ represents the noise matrix containing the i.i.d. additive white Gaussian noise (AWGN) components on N_s subcarriers, following the distribution $\mathcal{CN}(0, \sigma^2)$. Besides, $\mathbf{H}_{\rm s} = \text{diag}(\mathbf{H}_1, \ldots, \mathbf{H}_{N_s}) \in \mathbb{C}^{N_s K \times N_s N_t}$ is the effective channel matrix, and $\mathbf{H}_n$ $(n = 1, 2, \cdots, N_s)$ is the channel matrix on the nth subcarrier with

$$\mathbf{H}_n = \sum_{u=0}^{N_c} \tilde{\mathbf{H}}_u e^{-\frac{j2\pi u(n-1)}{N_s}}, \tag{6}$$

where $\tilde{\mathbf{H}}_u = \left[\tilde{\mathbf{h}}_{1,u}^{\rm T}, \ldots, \tilde{\mathbf{h}}_{K,u}^{\rm T}\right]^{\rm T} \in \mathbb{C}^{K \times N_t}$ represents the channel matrix at the uth tap, and $\tilde{\mathbf{h}}_{k,u}$ is the channel vector for the kth UE at the uth tap, and follows the distribution $\mathcal{CN}(\mathbf{0}, \frac{\mathbf{I}_{N_t}}{N_c+1})$ with i.i.d. Rayleigh fading coefficients. The corresponding channel for each UE on the nth subcarrier can be expressed as

$$\mathbf{h}_{k,n} = \sum_{u=0}^{N_c} \tilde{\mathbf{h}}_{k,u} e^{-\frac{j2\pi u(n-1)}{N_s}} \in \mathbb{C}^{1 \times N_t}. \tag{7}$$

For the considered DFRC MIMO-OFDM system, the transmitting radar beampattern at the detection angle θ can be expressed as $\frac{1}{N_s}\sum_{n=1}^{N_s} \mathbf{a}^{\rm H}(\theta)\mathbf{R}_n\mathbf{a}(\theta)$, representing the average over N_s subcarriers. Here, $\mathbf{a}(\theta) = [e^{-j\frac{N_t-1}{2}\pi\sin\theta}, e^{-j\frac{N_t-3}{2}\pi\sin\theta}, \cdots, e^{j\frac{N_t+1}{2}\pi\sin\theta}]^{\rm T} \in \mathbb{C}^{N_t \times 1}$ is the transmission steering vector, assuming an even number of transmit antennas on the DFRC-BS ULA and selecting the center of the ULA as the reference point. Furthermore, $\mathbf{R}_n$ stands for the effective spatial covariance matrix of the transmit DFRC MIMO-OFDM waveform on the nth subcarrier, defined as $\mathbf{R}_n = \frac{1}{L}\mathbf{G}_n\mathbf{G}_n^{\rm H}$. To ensure the positive definiteness of the covariance matrix $\mathbf{R}_n$, we assume that the frame length satisfies $L \geq N_t$, a condition will be easily achievable when considering broadband scenarios with approximately time-invariant channels.

Generally, traditional methods for designing DFRC waveforms aim to minimize the MUI energy to achieve effective communication. However, note that not all interference is detrimental. Thus, it is unnecessary to minimize all types of interference. Interference can be categorized into destructive interference (DI) and CI [38]. For QPSK case as illustrated in [38], CI is considered a beneficial disturbance because it directs the received signal towards the correct decision region, known as the constructive region. This redirection towards the constructive region provides additional degrees of freedom, making CI a valuable aspect.

The CI technology has been extensively studied in recent research [39] [40]. To avoid diverting our primary focus, we will not delve into the derivation of CI constraints. For the sake of derivation simplicity, we adopt a phase rotation approach to separate the amplitude and phase parts of the received signal. This strategy facilitates the disentanglement of interference signals from the received signal. We express the rotated noiseless received signal as $\hat{\mathrm{y}}_{k,n} = \hat{\mathbf{h}}_{k,n}\mathbf{x}_l = \Gamma_k + \hat{\mathrm{t}}_{k,n}$, where $\hat{\mathbf{h}}_{k,n} = \mathbf{h}_{k,n}e^{j\varphi_{k,n}}$, and $\hat{\mathrm{t}}_{k,n} = \hat{\mathbf{h}}_{k,n}\mathbf{x}_l - \Gamma_k$. This representation helps in managing interference signals while ensuring that the received signal remains within the constructive region.

By leveraging the geometric relationships of rotational QPSK symbols illustrated in Fig. 3, the constraints for constructing CI can be formulated as follows

$$\left|\text{Im}\left(\hat{\mathbf{h}}_{k,n}\mathbf{x}_l\right)\right| \leq \left(\text{Re}\left(\hat{\mathbf{h}}_{k,n}\mathbf{x}_l\right) - \Gamma_k\right)\tan\varphi, \forall k, \forall n, \tag{8}$$

where $\varphi = \frac{\pi}{\bar{M}}$ is the central angle, and $\bar{M}$ is the modulation order of the PSK scheme.

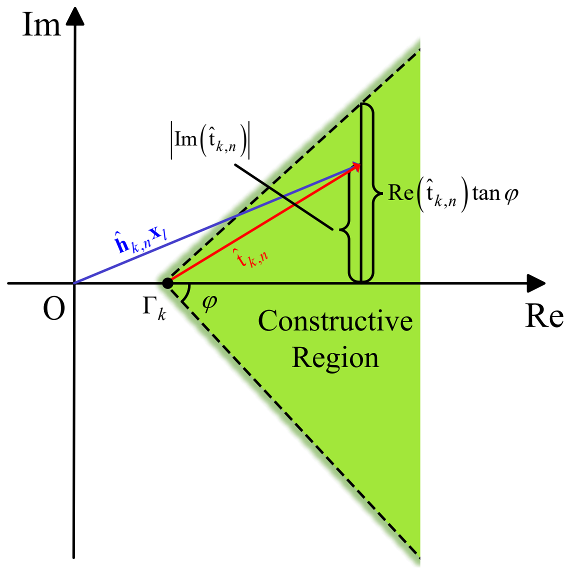

Fig. 3. Constructive region for a PSK constellation.

C. Sidelobe Level for Radar

To design our DFRC MIMO-OFDM waveform, we denote the ideal reference waveform as $\mathbf{G}_0 \triangleq (\mathbf{F}_{\mathrm{DFT}}^{\mathrm{H}} \otimes \mathbf{I}_{N_t})\mathbf{X}_{\mathrm{s},0}$, where $\mathbf{X}_{\mathrm{s},0}$ represents the radar waveform before the IDFT operation, capable of achieving an ideal detection probability. By employing directional beamforming techniques, we can achieve a benchmark waveform similar to $\mathbf{G}_0$. By employing directional beamforming design [26], a reference waveform $\mathbf{G}_0$ can be obtained. Thus, from the perspective of radar performance, it is beneficial to make the DFRC waveform $\mathbf{G} = \left(\mathbf{F}_{\mathrm{DFT}}^{\mathrm{H}} \otimes \mathbf{I}_{N_t}\right)\mathbf{X}_{\mathrm{s}}$ as close to $\mathbf{G}_0$ as possible.

To achieve lower sidelobe levels in the designed waveform, it is imperative to suppress clutter from adjacent range cells. This suppression is necessary to avoid some masking effect of strong targets on weaker ones. A commonly employed metric for quantifying range sidelobes and assessing their suppression is the weighted integrated sidelobe level (WISL), and defined as [41]

$$\mathrm{WISL} = \sum_{k=1}^{L-1} \omega_k |\mathrm{Tr}(\mathbf{U}_k \mathbf{x}\mathbf{x}^{\mathrm{H}})|^2. \tag{9}$$

where ω_k denotes the nonnegative weights,

$$\mathbf{U}_k\left(p,q\right) = \begin{cases} 1, & p-q=k \\ 0, & p-q\neq k \end{cases}, \tag{10}$$

and

$$\mathbf{x} = \mathrm{vec}(\mathbf{X}_{\mathrm{s}}). \tag{11}$$

Here, we introduce a more general norm-based metric, i.e., WPISL, for autocorrelation sidelobes, and set $\mathrm{e}_k = \mathrm{Tr}(\mathbf{U}_k\mathbf{x}\mathbf{x}^{\mathrm{H}})$. The definition of WPISL has

$$\mathrm{WPISL} = \sum_{k=1}^{L-1} \omega_k |\mathrm{e}_k|^p, \tag{12}$$

where $2 \leq p \leq +\infty$. Once $p=2$ we could get the WISL metric. If ω_k=1,$\forall k$, we could get the ISL metric. Furthermore, when both $p \to +\infty$ and $\omega_k = 1, \forall k$, we would get the $\left(\sum_{k=1}^{L-1} |\mathrm{e}_k|^p\right)^{1/p} \to \max_k \{|\mathrm{e}_k|\}$, which corresponds to the PSL metric.

III. An MM-based Integrated Waveform Design

A. Peak-to-Valley Power Ratio Constraint

In OFDM systems, the time-domain transmitted signal may exhibit significant peaks, leading to a high PAPR after performing IDFT operations on all subcarriers. This elevated PAPR not only diminishes the efficiency of power amplifiers in the transmitter but also reduces the signal-to-quantization noise ratio (SQNR) of analog-to-digital converters (ADCs) and DACs.

To ensure that amplifiers in the RF components operate in the saturation or nonlinear region, maximizing transmission power, transmitted waveforms are typically subject to constant envelope and PAPR constraints.

However, the CM constraint limits the flexibility of waveform design and system performance. The PAPR constraint with less stringent restricts the peak-to-average power ratio and is a key issue in OFDM systems [42]. PAPR, the ratio of maximum to average passband signal power, can lead to a large modulus dynamic range (MDR), requiring costly wide-range amplifiers and causing waveform distortion. To address this, based on [31]–[33], we also apply the peak-to-valley power ratio (PVPR) concept to the pre-coded waveform dynamic range, thereby compensating for the drawbacks of the PAPR constraint. This PVPR constraint is defined as

$$\mathrm{PVPR}(\mathbf{X}_{\mathrm{s}}) = \frac{\max\limits_{i,l} \left|\left[(\mathbf{F}^{\mathrm{H}} \otimes \mathbf{I}_{N_t})\mathbf{X}_{\mathrm{s}}\right]_{i,l}\right|^2}{\min\limits_{i,l} \left|\left[(\mathbf{F}^{\mathrm{H}} \otimes \mathbf{I}_{N_t})\mathbf{X}_{\mathrm{s}}\right]_{i,l}\right|^2} \leq \chi^2, \tag{13}$$

where χ is a parameter controlling the MDR of the waveform. Specifically, when the amplitude deviation is 0, this constraint is equivalent to a CM constraint with uniform amplitude. It is evident that the CM constraint is a specific case of the PVPR constraint.

B. Problem Formulation

Generally, radar in practical scenarios often necessitates transmission with utmost available power. Thus, we also impose the following power constraint, i.e., $\frac{1}{L}\left\|(\mathbf{F}^{\mathrm{H}} \otimes \mathbf{I}_{N_t})\mathbf{X}_{\mathrm{s}}\right\|_{\mathrm{F}}^2 \leq P_{\mathrm{t}}$, where the power budget P_{t} is entirely utilized for generating the DFRC MIMO-OFDM waveform. The concept of CI is adopted to enhance the performance of the DFRC waveform with a focus on minimizing low-range sidelobes. To achieve a better trade-off performance, admissible square WSE constraint (corresponding to the 2nd constraint in (14)). To address these considerations, this text introduces a novel approach that employs controlled waveform dynamic range and overall transmission energy constraints, aiming to alleviate the shortcomings associated with PAPR constraints. The problem under consideration can be formulated as follows

$$\begin{aligned}
&\min_{\mathbf{X}_s} \sum_{k=1}^{L-1} \omega_k \left|\mathrm{Tr}\left(\mathbf{U}_k \mathrm{vec}(\mathbf{X}_s)\left(\mathrm{vec}(\mathbf{X}_s)\right)^{\mathrm{H}}\right)\right|^p \\
&\text{s.t. } \frac{1}{L}\left\|\left(\mathbf{F}^{\mathrm{H}} \otimes \mathbf{I}_{N_t}\right)\mathbf{X}_s\right\|_F^2 \le P_t \\
&\quad \left\|(\mathbf{F}_{\mathrm{DFT}}^{\mathrm{H}} \otimes \mathbf{I}_{N_t})\mathbf{X}_s - \mathbf{G}_0\right\|_F^2 \le \delta^2 \\
&\quad \left|\mathrm{Im}\left(\hat{\mathbf{h}}_{k,n}\mathbf{x}_l\right)\right| \le \left(\mathrm{Re}\left(\hat{\mathbf{h}}_{k,n}\mathbf{x}_l\right) - \Gamma_k\right)\tan\varphi \\
&\quad \frac{\max\limits_{i,l}\left|\left[\left(\mathbf{F}^{\mathrm{H}} \otimes \mathbf{I}_{N_t}\right)\mathbf{X}_s\right]_{i,l}\right|^2}{\min\limits_{i,l}\left|\left[\left(\mathbf{F}^{\mathrm{H}} \otimes \mathbf{I}_{N_t}\right)\mathbf{X}_s\right]_{i,l}\right|^2} \le \chi^2.
\end{aligned} \tag{14}$$

C. Proposed MM-Based Method

In MIMO radar waveform design, solving problem (14) presents significant challenges due to the non-convex nature of the optimization involved. The major difficulty arises from the complex cyclic autocorrelation and cross-correlation expressions, specifically e_k, which involve DFT and a selection matrix. To tackle this non-convex waveform design issue, we adopt the Majorization-Minimization (MM) framework. The MM algorithm transforms the original problem into a more manageable form by deriving an upper bound surrogate function that approximates the objective function locally at each iteration. This surrogate function is then minimized in the subsequent iteration, enabling efficient convergence towards a solution.

To obtain the substitute function for $|\mathrm{e}_k|^p, (k = 1, ..., L-1)$, we present *Lemma 1* as follows.

Lemma 1 [41] : Let the function $v(x) = x^p$, where $p \ge 2$ and $x \in [0, \bar{x}]$. For any given $x_0 \in [0, \bar{x})$, The relationship is as follows

$$v(x) \le ax^2 + bx + \tilde{c}, \tag{15}$$

where

$$a = \frac{\bar{x}^p - x_0^p - p x_0^{p-1}(\bar{x} - x_0)}{(\bar{x} - x_0)^2}, \tag{16}$$

$$b = p x_0^{p-1} - 2a x_0. \tag{17}$$

Without confusion, we will use $\tilde{c}$ to absorb terms unrelated to optimization.

Specifically, to address problem of (14), we turn to using MM framework, and construct an objective optimization function. Given the qth iteration's value of $\left|(\mathrm{e}_k)^{(q)}\right|$, according to *Lemma 1*, know that $|\mathrm{e}_k|^p$ is majorized at $\left|(\mathrm{e}_k)^{(q)}\right|$ over $[0, \tilde{x}_0]$ by

$$\mathcal{J}_k|\mathrm{e}_k|^2 + \mathfrak{K}_k|\mathrm{e}_k| + \mathcal{J}_k\left|(\mathrm{e}_k)^{(q)}\right|^2 - (p-1)\left|(\mathrm{e}_k)^{(q)}\right|^p, \tag{18}$$

where

$$\mathcal{J}_k = \frac{\tilde{x}_0^p - \left|(\mathrm{e}_k)^{(q)}\right|^p}{\left(\tilde{x}_0 - \left|(\mathrm{e}_k)^{(q)}\right|\right)^2} - \frac{p\left|(\mathrm{e}_k)^{(q)}\right|^{p-1}}{\left(\tilde{x}_0 - \left|(\mathrm{e}_k)^{(q)}\right|\right)}, \tag{19}$$

$$\mathfrak{K}_k = p\left|(\mathrm{e}_k)^{(q)}\right|^{p-1} - 2\mathcal{J}_k\left|(\mathrm{e}_k)^{(q)}\right|. \tag{20}$$

For the sake of convenience, we define $f(\mathbf{x}) = \sum_{k=1}^{L-1}\omega_k|\mathrm{e}_k|^p$ and obtain

$$f(\mathbf{x}) \le \sum_{k=1}^{L-1}\omega_k\left(\mathcal{J}_k|\mathrm{e}_k|^2 + \mathfrak{K}_k|\mathrm{e}_k| + \tilde{c}\right). \tag{21}$$

We further observe that $\mathfrak{K}_k \le 0$ and

$$|e_k|\left|(e_{-k})^{(q)}\right| \ge \mathrm{Re}\left[e_k \cdot (e_{-k})^{(q)}\right]. \tag{22}$$

Therefore, we have

$$\begin{aligned}
f(\mathbf{x}) \le &\sum_{k=1}^{L-1}\omega_k\mathcal{J}_k|\mathrm{e}_k|^2 \\
&+ \sum_{k=1}^{L-1}\omega_k\mathfrak{K}_k\mathrm{Re}\left\{e_k^*\frac{e_k^{(q)}}{\left|e_k^{(q)}\right|}\right\} + \sum_{k=1}^{L-1}\omega_k\tilde{c},
\end{aligned} \tag{23}$$

where

$$\begin{aligned}
&\sum_{k=1}^{L-1}\omega_k\mathfrak{K}_k\mathrm{Re}\left\{e_k^*\frac{e_k^{(q)}}{\left|e_k^{(q)}\right|}\right\} \\
&= \sum_{k=1}^{L-1}\omega_k\mathfrak{K}_k\mathrm{Re}\left\{\mathrm{Tr}(\mathbf{U}_{-k}\mathbf{x}\mathbf{x}^{\mathrm{H}})\frac{e_k^{(q)}}{\left|e_k^{(q)}\right|}\right\} \\
&= \mathrm{Re}\left\{\mathbf{x}^{\mathrm{H}}\left(\sum_{k=1}^{L-1}\omega_k\mathfrak{K}_k\frac{e_k^{(q)}}{\left|e_k^{(q)}\right|}\mathbf{U}_{-k}\right)\mathbf{x}\right\} \\
&= \frac{1}{2}\mathbf{x}^{\mathrm{H}}\left(\sum_{k=1-L}^{L-1}\omega_k\mathfrak{K}_k\frac{e_{-k}^{(q)}}{\left|e_{-k}^{(q)}\right|}\mathbf{U}_k\right)\mathbf{x},
\end{aligned} \tag{24}$$

with $\mathrm{e}_{-k} = \mathrm{Tr}(\mathbf{U}_{-k}\mathbf{x}\mathbf{x}^{\mathrm{H}})$. In (23), it can be observed that there remains a challenging quartic term $\sum_{k=1}^{L-1}\omega_k\mathcal{J}_k|\mathrm{e}_k|^2$. We optimize it through its maximum eigenvalue, as stated in the following lemma.

Lemma 2 [43] : The function $d(\mathbf{x}) = \sum_{k=1}^{L-1}\omega_k\mathcal{J}_k|\mathrm{e}_k|^2 + \frac{1}{2}\mathbf{x}^{\mathrm{H}}\left(\sum_{k=1-L}^{L-1}\omega_k\mathfrak{K}_k\frac{e_{-k}^{(q)}}{\left|e_{-k}^{(q)}\right|}\mathbf{U}_k\right)\mathbf{x}$ is majorized by

$$u(\mathbf{x}) = \lambda_{\max}(\mathcal{L})\|\mathbf{x}\|_2^2 - 2\lambda_{\max}(\mathcal{L})\,\mathrm{Re}\left[\mathbf{y}^{\mathrm{H}}\mathbf{x}\right] + \tilde{c}, \tag{25}$$

where

$$\mathcal{L} = \sum_{k=1-L}^{L-1}\frac{p}{2}\omega_k\left|(\mathrm{e}_k)^{(q)}\right|^{p-2}(\mathrm{e}_{-k})^{(q)}\mathbf{U}_k, \tag{26}$$

$$\mathbf{y} = \left(1 + \frac{\lambda_{\max}(\mathfrak{B})}{\lambda_{\max}(\mathcal{L})}\left\|\mathbf{x}^{(q)}\right\|_2^2\right)\mathbf{x}^{(q)} - \frac{1}{\lambda_{\max}(\mathcal{L})}\mathcal{L}\mathbf{x}^{(q)}. \tag{27}$$

Proof: See Appendix A for the detailed derivation. ■

In steps (21) to (25), we have constructed an auxiliary function and derived update rules to progressively simplify the objective function. These steps lay the foundation for accelerated convergence. To further enhance the convergence speed during the iterative process, we can adopt the acceleration scheme based on the squared iterative method (SQUAREM) proposed in [41]. The SQUAREM method introduces momentum terms to achieve quadratic convergence, significantly reducing the number of iterations and making the iterative updates more efficient. To further facilitate optimization, we shall transform problem (14) into its equivalent vector form, as follows

$$\begin{aligned}
\min_{\mathbf{X}_\mathrm{s}}\ & \lambda_{\max}(\mathcal{L})\left\|\mathrm{vec}(\mathbf{X}_\mathrm{s})\right\|_2^2-2\lambda_{\max}(\mathcal{L})\,\mathrm{Re}\left[\mathbf{y}^\mathrm{H}\mathrm{vec}(\mathbf{X}_\mathrm{s})\right]\\
\text{s.t. }& \frac{1}{L}\left\|\left(\mathbf{F}^\mathrm{H}\otimes\mathbf{I}_{N_t}\right)\mathbf{X}_\mathrm{s}\right\|_\mathrm{F}^2\le P_\mathrm{t}\\
& \left\|\left(\mathbf{F}_\mathrm{DFT}^\mathrm{H}\otimes\mathbf{I}_{N_t}\right)\mathbf{X}_\mathrm{s}-\mathbf{G}_0\right\|_\mathrm{F}^2\le\delta^2\\
& \left|\mathrm{Im}\left(\hat{\mathbf{h}}_{k,n}\mathbf{x}_l\right)\right|\le\left(\mathrm{Re}\left(\hat{\mathbf{h}}_{k,n}\mathbf{x}_l\right)-\Gamma_k\right)\tan\varphi\\
& \frac{\max_{i,l}\left|\left[\left(\mathbf{F}^\mathrm{H}\otimes\mathbf{I}_{N_t}\right)\mathbf{X}_\mathrm{s}\right]_{i,l}\right|^2}{\min_{i,l}\left|\left[\left(\mathbf{F}^\mathrm{H}\otimes\mathbf{I}_{N_t}\right)\mathbf{X}_\mathrm{s}\right]_{i,l}\right|^2}\le\chi^2.
\end{aligned}\tag{28}$$

where $\mathbf{x}_l$ is the part of $\mathbf{X}_\mathrm{s}$ that corresponds to the transmitted data from all antennas during the l-th OFDM symbol period. Since the PVPR constraint is nonlinear and non-convex, the above problem is exceedingly challenging to be solved. To handle this difficulty, we propose to deal with the PVPR constraint as presented in *Lemma 3* as follows.

Lemma 3 : The optimization problem (28) can be relaxed into the following optimization problem

$$\begin{aligned}
\min_{\mathbf{X}_\mathrm{s},\beta}\ & \lambda_{\max}(\mathcal{L})\left\|\mathrm{vec}(\mathbf{X}_\mathrm{s})\right\|_2^2-2\lambda_{\max}(\mathcal{L})\,\mathrm{Re}\left[\mathbf{y}^\mathrm{H}\mathrm{vec}(\mathbf{X}_\mathrm{s})\right]\\
\text{s.t. }& \frac{1}{L}\left\|\left(\mathbf{F}^\mathrm{H}\otimes\mathbf{I}_{N_t}\right)\mathbf{X}_\mathrm{s}\right\|_\mathrm{F}^2\le P_\mathrm{t}\\
& \left\|\left(\mathbf{F}_\mathrm{DFT}^\mathrm{H}\otimes\mathbf{I}_{N_t}\right)\mathbf{X}_\mathrm{s}-\mathbf{G}_0\right\|_\mathrm{F}^2\le\delta^2\\
& \left|\mathrm{Im}\left(\hat{\mathbf{h}}_{k,n}\mathbf{x}_l\right)\right|\le\left(\mathrm{Re}\left(\hat{\mathbf{h}}_{k,n}\mathbf{x}_l\right)-\Gamma_k\right)\tan\varphi\\
& \beta\le\left|\left[(\mathbf{F}^\mathrm{H}\otimes\mathbf{I}_{N_t})\mathbf{X}_\mathrm{s}\right]_{i,l}\right|^2\le\beta\chi^2.
\end{aligned}\tag{29}$$

Proof: First of all, by defining an auxiliary variable $\beta=\min_{i,l}\left|\left[\left(\mathbf{F}^\mathrm{H}\otimes\mathbf{I}_{N_t}\right)\mathbf{X}_\mathrm{s}\right]_{i,l}\right|^2$, the PVPR constraint (i.e., the last constraint in (28)) can be reformulated as

$$\begin{cases}\beta=\min_{i,l}\left|\left[\left(\mathbf{F}^\mathrm{H}\otimes\mathbf{I}_{N_t}\right)\mathbf{X}_\mathrm{s}\right]_{i,l}\right|^2\\ \max_{i,l}\left|\left[\left(\mathbf{F}^\mathrm{H}\otimes\mathbf{I}_{N_t}\right)\mathbf{X}_\mathrm{s}\right]_{i,l}\right|^2\le\beta\chi^2,\end{cases}\tag{30}$$

which is equivalent to

$$\begin{aligned}
\beta&=\min_{i,l}\left|\left[\left(\mathbf{F}^\mathrm{H}\otimes\mathbf{I}_{N_t}\right)\mathbf{X}_\mathrm{s}\right]_{i,l}\right|^2\\
&\le\left|\left[\left(\mathbf{F}^\mathrm{H}\otimes\mathbf{I}_{N_t}\right)\mathbf{X}_\mathrm{s}\right]_{i,l}\right|^2\\
&\le\max_{i,l}\left|\left[\left(\mathbf{F}^\mathrm{H}\otimes\mathbf{I}_{N_t}\right)\mathbf{X}_\mathrm{s}\right]_{i,l}\right|^2\\
&\le\beta\chi^2.
\end{aligned}\tag{31}$$

Therefore, problem (28) can be equivalently reformulated as

$$\begin{aligned}
\min_{\mathbf{X}_\mathrm{s},\beta}\ & \lambda_{\max}(\mathcal{L})\left\|\mathrm{vec}(\mathbf{X}_\mathrm{s})\right\|_2^2-2\lambda_{\max}(\mathcal{L})\,\mathrm{Re}\left[\mathbf{y}^\mathrm{H}\mathrm{vec}(\mathbf{X}_\mathrm{s})\right]\\
\text{s.t. }& \frac{1}{L}\left\|\left(\mathbf{F}^\mathrm{H}\otimes\mathbf{I}_{N_t}\right)\mathbf{X}_\mathrm{s}\right\|_\mathrm{F}^2\le P_\mathrm{t}\\
& \left\|\left(\mathbf{F}_\mathrm{DFT}^\mathrm{H}\otimes\mathbf{I}_{N_t}\right)\mathbf{X}_\mathrm{s}-\mathbf{G}_0\right\|_\mathrm{F}^2\le\delta^2\\
& \left|\mathrm{Im}\left(\hat{\mathbf{h}}_{k,n}\mathbf{x}_l\right)\right|\le\left(\mathrm{Re}\left(\hat{\mathbf{h}}_{k,n}\mathbf{x}_l\right)-\Gamma_k\right)\tan\varphi\\
& \beta\le\left|\left[(\mathbf{F}^\mathrm{H}\otimes\mathbf{I}_{N_t})\mathbf{X}_\mathrm{s}\right]_{i,l}\right|^2\le\beta\chi^2\\
& \beta=\min_{i,l}\left|\left[\left(\mathbf{F}^\mathrm{H}\otimes\mathbf{I}_{N_t}\right)\mathbf{X}_\mathrm{s}\right]_{i,l}\right|^2.
\end{aligned}\tag{32}$$

Then we relax problem (32) by removing the last constraint, resulting in the optimization problem (29). ■

The non-convexity introduced by the fourth constraint in problem (29) poses substantial challenges for direct solution approaches, complicating the optimization landscape and potentially leading to local optima. To address these challenges and leverage the advantages of convex optimization, we undertake a deliberate relaxation of the problem structure. Through careful manipulation of the constraints and objectives, we derive a convex formulation of the problem, as outlined in *Lemma 4*.

Lemma 4 : The optimization problem (29) can be further relaxed into the following

$$\begin{aligned}
\min_{\mathbf{X}_\mathrm{s},\beta,\mathbf{Z}}\ & \lambda_{\max}(\mathcal{L})\left\|\mathrm{vec}(\mathbf{X}_\mathrm{s})\right\|_2^2-2\lambda_{\max}(\mathcal{L})\,\mathrm{Re}\left[\mathbf{y}^\mathrm{H}\mathrm{vec}(\mathbf{X}_\mathrm{s})\right]\\
\text{s.t. }& \frac{1}{L}\left\|\left(\mathbf{F}^\mathrm{H}\otimes\mathbf{I}_{N_t}\right)\mathbf{X}_\mathrm{s}\right\|_\mathrm{F}^2\le P_\mathrm{t}\\
& \left\|\left(\mathbf{F}_\mathrm{DFT}^\mathrm{H}\otimes\mathbf{I}_{N_t}\right)\mathbf{X}_\mathrm{s}-\mathbf{G}_0\right\|_\mathrm{F}^2\le\delta^2\\
& \left|\mathrm{Im}\left(\hat{\mathbf{h}}_{k,n}\mathbf{x}_l\right)\right|\le\left(\mathrm{Re}\left(\hat{\mathbf{h}}_{k,n}\mathbf{x}_l\right)-\Gamma_k\right)\tan\varphi\\
& \beta\mathbf{1}_{NN_tL}\le\mathrm{diag}(\mathbf{Z})\le\beta\chi^2\mathbf{1}_{NN_tL}\\
& \mathbf{Z}\succeq\mathbf{0}.
\end{aligned}\tag{33}$$

Proof: See Appendix B for the detailed derivation. ■

It is easy to check that (33) is convex, and can be solved by standard numerical tools, e.g., the CVX toolbox [44].

IV. Numerical Simulation

In this section, we mainly formulate a uniform linear array configuration for both the transmitting arrays and receiving ones. The elements in these arrays are all uniformly spaced with half a wavelength interval. In the following simulation (unless otherwise specified), the number of transmitting antennas is $N_t=16$, and the code-length of the waveform is $L=512$. We suppose that $P_\mathrm{t}=1$, the length of the CP is 3 and with a total of 32 subcarriers available. Moreover, there are 2 active UEs and 3 designated targets within our experimental scenario. Additionally, we set the constellation selected for communication users as the unit-power QPSK manner. Therein, we also try to employ Monte Carlo trials to assess the statistical performance of algorithms for designing

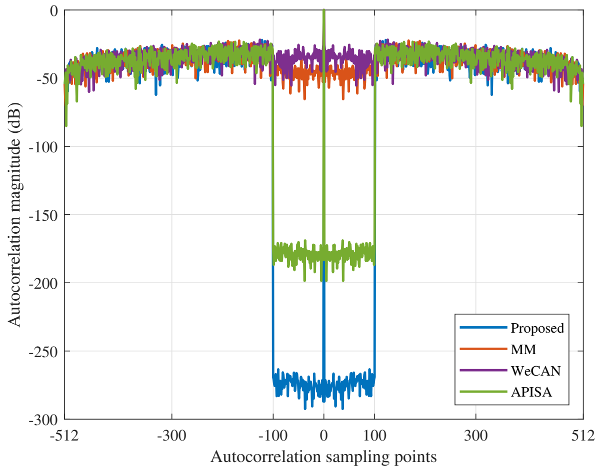

Fig. 4. ACL comparison for suppressing sidelobes in the single area.

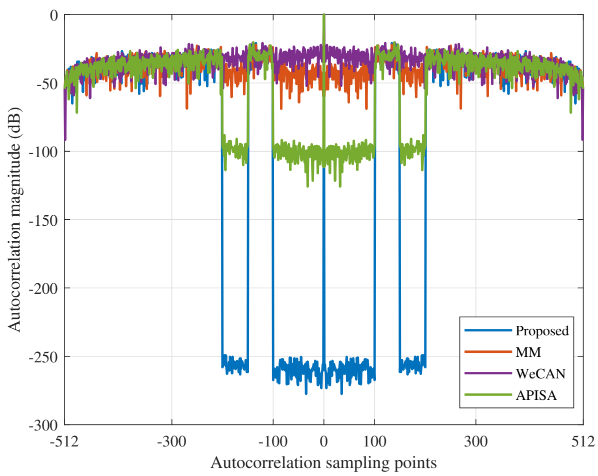

Fig. 5. ACL comparison for suppressing sidelobes for multiple areas.

waveforms. Genereally, the definition of the auto-correlation level (ACL) can be denoted by

$$\mathrm{ACL} = 20\log_{10}\frac{|\mathrm{e}_k|}{|\mathrm{e}_0|}(\mathrm{dB}), \tag{34}$$

A. *Sublobe Level Suppression*

To validate the radar's performance, we further define the averaging consumption time, the averaging autocorrelation magnitude within the inhibitory range as Aver-time and Aver-ACL, respectively. In this subsecion, we consider the scenario for suppressing single-sidelobe region with weights $\omega_k = 1$, $k \in \{1, 2, ..., 100\}$ and $p = 2$. In Table I and Fig. 4, we have compared our algorithm (referred to as "Proposed") with WeCAN [45], APISA [46], and MM [47]. For the MM algorithm, this study addresses more complex scenarios with additional constraints and a different descent mechanism, enhancing its applicability and performance in various conditions. Here, the metric, i.e., ACL in the suppression region, is defined similar to [48]. All experiments were performed on a PC with a 2.30 GHz i7-12700H CPU and 16GB RAM. After running 1000 iterations, MM algorithm has achieved an ACL of -51 dB, WeCAN obtained ACL of -42 dB, respectively. Additionally, APISA with an alternating projection mechanism has achieved ACL values of -187 dB. Our proposed algorithm achieved an ACL of -283 dB.

TABLE I
PERFORMANCE OF SINGLE-AREA SIDELOBE SUPPRESSION

Algorithms	Multiple Area	
	Aver-ACL (dB)	**Aver-time (s)**
WeCAN	-42	22.74
MM	-51	0.83
APISA	-187	0.33
Proposed	-283	0.24

TABLE II
PERFORMANCE OF MULTIPLE-AREA SIDELOBE SUPPRESSION

Algorithms	Multiple Area	
	Aver-ACL (dB)	**Aver-time (s)**
WeCAN	-38	25.74
MM	-49	0.86
APISA	-103	0.32
Proposed	-258	0.25

Additionally, we also considered the sidelobe suppression in multi-region scenarios, specifically setting weights $\omega_k = 1$, $k \in \{1, 2, ..., 100\} \cup \{150, 151, ..., 200\}$. In Table II and Fig. 5, we have observed some outstanding performance in both runtime and ACL metric, where Table II also presents similar characteristics to Table I. The proposed algorithm in this paper achieved the best results in all 20 Monte Carlo trials.

To further evaluate the computational complexity, we demonstrate convergence metric v.s. the number of iterations in Fig. 6, and CPU time consumption in Table I. Therein, in Fig. 6, we employ $\log\left|\mathbf{x}^{(q)} - \mathbf{x}^{(q-1)}\right|$ as the convergence metric in the y-axis, with a threshold value 10^{-10}. The figure reveals obvious convergence differences, where our algorithm consumes much less time than MM, APISA, and WeCAN, and exhibits superior robustness. Meanwhile, as indicated in Table I and Fig. 6, WeCAN exhibits slower convergence, APISA exhibits oscillations which might attribute to their alternating projections disabled for thus non-convex cases.

Additionally, we assess the performance in minimizing PSL, by setting p to a large value, $\omega_k = 1, \forall k$, so as to yield an approximate PSL. Here, various p values were considered $p = 10, 50, 10^2$, and 10^3, with a maximum iteration number 4×10^4. As shown in Fig. 7, it is evident that for smaller p values (e.g., $p = 10$), the convergence is correspondingly rapid, even with a higher PSL. Conversely, for larger p values (e.g., $p = 10^3$), the situation is reversed. Hence, an incremental approach for p can be employed to attain lower PSL and change convergence.

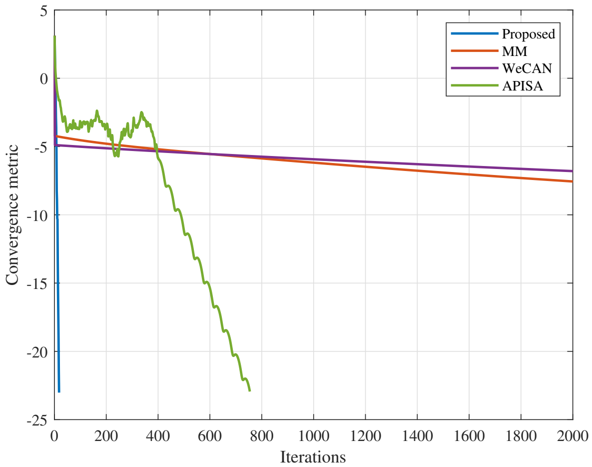

Fig. 6. Convergence comparison of different methods.

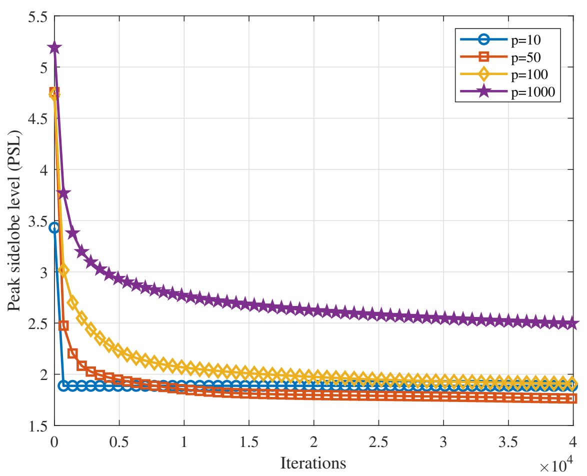

Fig. 7. The evolution curves of the peak sidelobe level.

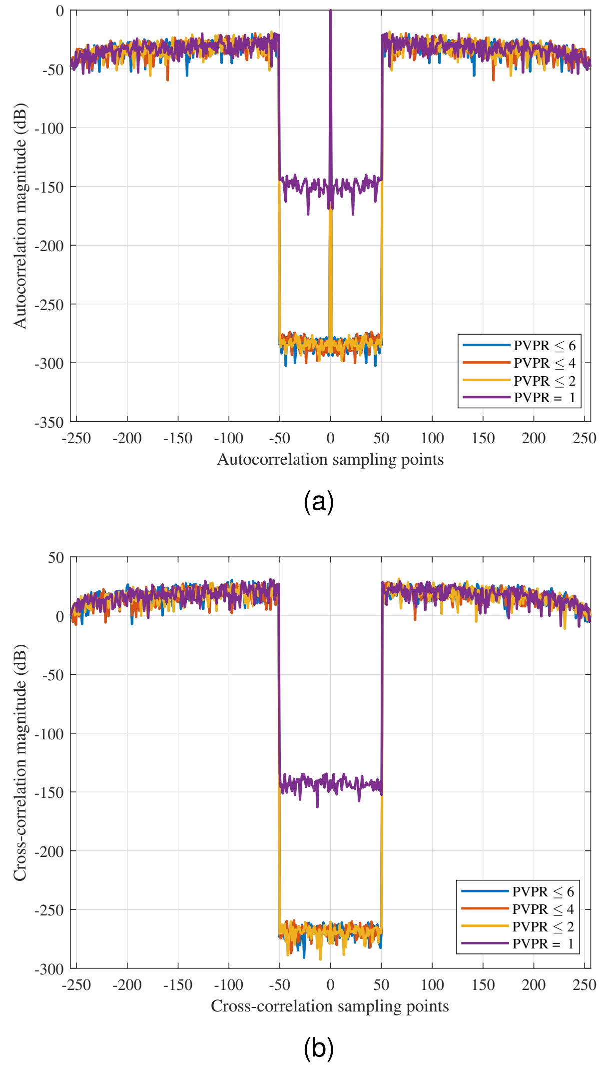

Fig. 8. Autocorrelation (top) and cross-correlation (bottom) plots of waveforms under different PVPR constraints.

B. Effect of PVPR

In this subsection, we would delve into the impact of aforementioned PVPR constraint on the inhibition of local-correlation. Here, we mainly employ the proposed algorithm to synthesize low-correlation waveforms within an extended local delay range of [-50, 50] and $L = 256$ for various PVPR constraints. Namely, we tried to relax the constant model (PVPR=1) gradually to other PVPR constraints, such as PVPR≤2, PVPR≤4, and PVPR≤6. Accordingly, Fig. 8(a) has illustrated the resulting waveform correlation levels under different PVPR constraints. It is evident that from the CM constraint to a slightly relaxed PVPR≤2 constraint, the local waveform correlation level decreases from around -150 dB to nearly -300 dB. Subsequently, as we gradually relax the PVPR constraint from PVPR≤2 to PVPR≤6, we observe minimal variation in the local waveform correlation level, hovering around -300 dB. We can infer that the waveforms synthesized by the algorithm in this study attain a low correlation level. Furthermore, Fig. 8(b) illustrates the intercorrelation levels of the designed waveforms. It is discernible from the figure that as the PVPR constraints being relaxed, both the sidelobes of local autocorrelation and the intercorrelation levels of designed waveforms can approximately approach -300 dB. This substantiates the algorithm's capability to design nearly orthogonal local low-correlation transmission waveforms. Additionally, Fig. 9(a)-(d) have illustrated the normalized amplitude distribution of designed waveforms in these four scenarios. It can be observed that the case of PVPR = 2 could maintain the dynamic range of each antenna's amplitude within acceptable fluctuations, whereas PAPR = 2 constraint results in a larger range. This instance highlights that the proposed PVPR constraint could stand as the preferred manner for enhancing transmitter's efficiency.

Furthermore, in Fig. 10, we have provided a comparison of the blur functions for the optimized waveforms. Fig. 10(a) illustrates the blur function for the traditional LFM-based integrated waveform. It is evident that in the temporal slices at any Doppler shift, there are relatively high sidelobe levels near the zero-delay point. In contrast, Fig. 10(b) depicts the region

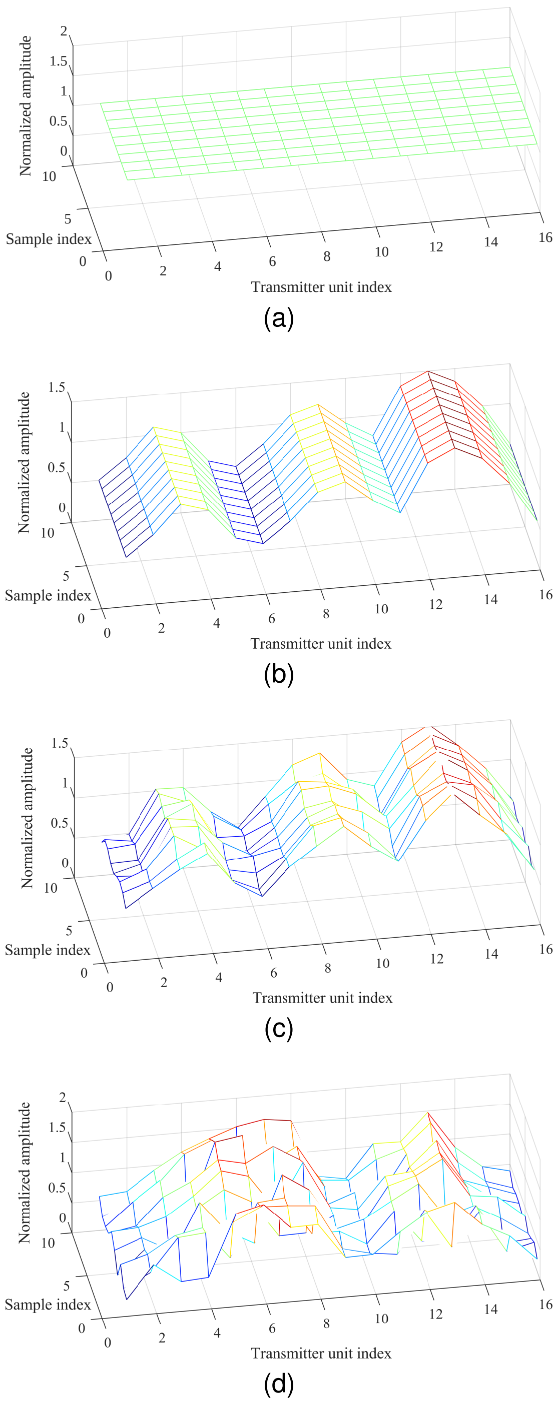

Fig. 9. Normalized transmit waveform amplitude distribution [29].(a) CM. (b) PVPR=1. (c) PVPR=2. (d) PAPR=2.

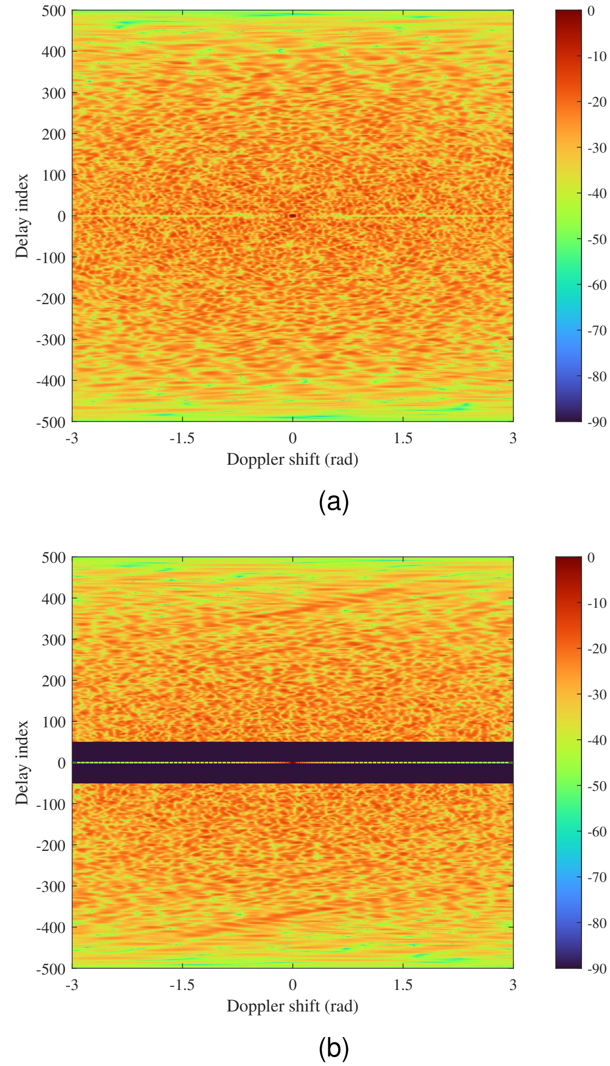

Fig. 10. Comparison of non-periodic waveform ambiguity function. (a) Integrated waveform based on the LFM. (b) The integrative waveform proposed in this paper.

of interest within the temporal slice, i.e, [-50, 50] optimized by the proposed algorithm, with the remarkably low sidelobe levels even below -90 dB. Consequently, the integrated waveform optimized in this study outperforms traditional LFM-based integrated waveforms in terms of ranging performance. To achieve target detection over a broader range of interest delays, future research can focus on the design of integrated waveforms with favorable autocorrelation characteristics across the entire delay range.

In the following figures, we mainly considered four different PVPR thresholds, i.e., 0.5, 1, 3, and 5. In Fig. 11, we assume $K = 4$, $\Gamma_k = 5\,\text{dB}, \forall k$, and SNR $= \frac{P_t}{\sigma^2}$ varies from 0 dB to 25 dB. As the SNR increases, all schemes gradually seem to be saturated. The phenomenon might attribute to the finite signal power, wherein the noise power becomes progressively negligible with a higher SNR, thus rendering MUI as the predominant factor. As the SNR increasing, the SER experiences a decline, and the influence of PVPR constraints on SER performance becomes more evident. This intricate interplay highlights the significance for managing PVPR in the context of evolving SNR conditions.

C. Communication-Radar Performance Trade-off

We further assessed the superiority of the proposed CI-based waveform design method through numerical results. For comparison purposes, the CI-based method and the LS-based method introduced in [26] are denoted as "CI" and "LS," respectively. The spatial covariance matrix $\mathbf{R}$ was obtained using the classical LS method from [49]. As shown in Fig. 12,

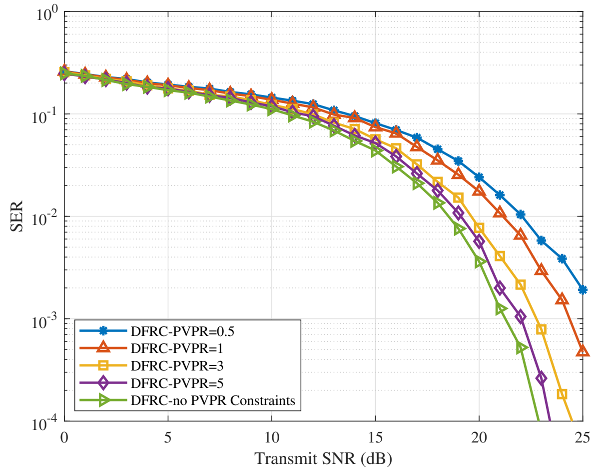

Fig. 11. SER performance versus transmit SNR with δ^2=2.

we begin by showcasing radar beampatterns derived through various waveform design methods. All presented results are normalized with respect to the omnidirectional radar beampattern, referred to as "Omni" for reference. When the square root of the WSE constraint reaches 3, it signifies that the designed beams accurately align with the target angles, with acceptable performance degradation. This observation underscores the effectiveness of all CI-based methods employed. The findings indicate that these methods consistently demonstrate their efficacy, affirming their capability to precisely point to target angles while maintaining satisfactory performance levels.

V. Conclusion and Future Works

This paper has addressed the challenges of mitigating the high PAPR problem of OFDM-based waveforms in a MIMO-DFRC system. Introducing a PVPR constraint, our approach enhances waveform fidelity and power control adaptability to real hardware conditions. The joint design of low-PVPR DFRC MIMO-OFDM waveforms, coupled with optimized radar and communication segments, has demonstrated superior performance. Key findings include improved control over waveform dynamic range, significant reduction in radar sidelobes, and enhanced communication efficiency with lower SER and higher average achievable rates. The MM framework has proven effective in transforming the non-convex problem into a series of convex ones, solvable via convex optimization techniques, thereby outperforming existing methods.

Future efforts should prioritize the practical implementation of the proposed low-PVPR waveforms in real-world MIMO-DFRC systems. This includes designing and testing prototypes across diverse operational environments to substantiate performance enhancements. Moreover, expanding performance metrics to encompass factors such as power consumption, latency, and robustness to interference will offer a more comprehensive evaluation of DFRC system effectiveness.

Appendix A

The quartic term $\sum_{k=1}^{L-1}\omega_k\mathcal{J}_k\left|\mathrm{e}_k\right|^2$ can be further rewritten using the vec notation as follows

$$\frac{1}{2}vec^{\mathrm{H}}\left(\mathbf{x}\mathbf{x}^{\mathrm{H}}\right)\cdot\mathfrak{B}\cdot\mathrm{vec}\left(\mathbf{x}\mathbf{x}^{\mathrm{H}}\right), \tag{35}$$

where $\mathfrak{B}=\sum_{k=1-L}^{L-1}\omega_k\mathcal{J}_k\mathrm{vec}\left(\mathbf{U}_{-k}\right)vec^{\mathrm{H}}\left(\mathbf{U}_{-k}\right)$. Furthermore, with respect to (35), we can proceed with the deduction to obtain

$$\begin{aligned}
&\frac{1}{2}\mathrm{vec}^{\mathrm{H}}(\mathbf{x}\mathbf{x}^{\mathrm{H}})\cdot\mathfrak{B}\cdot\mathrm{vec}(\mathbf{x}\mathbf{x}^{\mathrm{H}})\\
&\le\frac{1}{2}\lambda_{\max}(\mathfrak{B})\mathrm{vec}^{\mathrm{H}}(\mathbf{x}\mathbf{x}^{\mathrm{H}})\mathrm{vec}(\mathbf{x}\mathbf{x}^{\mathrm{H}})\\
&\quad+\mathrm{Re}\left[\mathrm{vec}^{\mathrm{H}}(\mathbf{x})^{(q)}(\mathbf{x}^{\mathrm{H}})^{(q)}\cdot(\mathfrak{B}-\lambda_{\max}(\mathfrak{B})\mathbf{I})\mathrm{vec}(\mathbf{x}\mathbf{x}^{\mathrm{H}})\right]+\tilde{c}\\
&\le\frac{1}{2}\lambda_{\max}(\mathfrak{B})\|\mathbf{x}\|_2^4\\
&\quad+\mathbf{x}^{\mathrm{H}}\left(\sum_{k=1-L}^{L-1}w_k\mathcal{J}_k e_{-k}(\mathbf{x}^{(q)})\mathbf{U}_k\right.\\
&\quad\left.-\lambda_{\max}(\mathfrak{B})\mathbf{x}^{(q)}\mathbf{x}^{(q)\mathrm{H}}\right)\mathbf{x}+\tilde{c}.
\end{aligned} \tag{36}$$

Furthermore, we can rewrite the right-hand side of inequality (23) as

$$\begin{aligned}
&\frac{1}{2}\lambda_{\max}(\mathfrak{B})\|\mathbf{x}\|_2^4\\
&\qquad+\mathbf{x}^{\mathrm{H}}\left(\mathcal{L}-\lambda_{\max}(\mathfrak{B})\mathbf{x}^{(q)}\mathbf{x}^{(q)\mathrm{H}}\right)\mathbf{x}+\tilde{c},
\end{aligned} \tag{37}$$

where

$$\mathcal{L}=\sum_{k=1-L}^{L-1}\frac{p}{2}\omega_k\left|(\mathrm{e}_k)^{(q)}\right|^{p-2}(\mathrm{e}_{-k})^{(q)}\mathbf{U}_k. \tag{38}$$

Let $\mathcal{L}_k=\left|(\mathrm{e}_k)^{(q)}\right|^{p-2}(\mathrm{e}_{-k})^{(q)}\mathbf{U}_k$. According to Theorem in [50], it is known that

$$\lambda_{\max}(\mathcal{L}_k)\leqslant\begin{cases}\sqrt{\frac{2(L-z)(L-1)}{L}}\mathrm{e}_k{}^{(q)}, z\neq0\\ 2L, z=0\end{cases}. \tag{39}$$

where z represents the range and $z=\lfloor\frac{2k}{L}\rfloor$.

Therefore, $\lambda_{\max}(\mathcal{L})$ also serves as an upper bound for the eigenvalues of the matrix $\mathcal{L}-\lambda_{\max}(\mathfrak{B})\mathbf{x}^{(q)}\mathbf{x}^{(q)\mathrm{H}}$; however, the computational complexity of obtaining $\lambda_{\max}(\mathcal{L}-\lambda_{\max}(\mathfrak{B})\mathbf{x}^{(q)}\mathbf{x}^{(q)\mathrm{H}})\mathbf{I}$ is comparatively higher. Therefore, we opt for $\lambda_{\max}(\mathcal{L})$ as the upper bound for $\mathcal{L}-\lambda_{\max}(\mathfrak{B})\mathbf{x}^{(q)}\mathbf{x}^{(q)\mathrm{H}}$, and $\lambda_{\max}(\mathfrak{B})\ge0$, we obtain

$$\begin{aligned}
&\mathbf{x}^{\mathrm{H}}\left(\mathcal{L}-\lambda_{\max}(\mathfrak{B})\mathbf{x}^{(q)}\mathbf{x}^{(q)\mathrm{H}}\right)\mathbf{x}\\
&\le\lambda_{\max}(\mathcal{L})\mathbf{x}^{\mathrm{H}}\mathbf{x}+\\
&2\,\mathrm{Re}\left[\mathbf{x}^{\mathrm{H}}\left(\mathcal{L}-\lambda_{\max}(\mathfrak{B})\mathbf{x}^{(q)}\mathbf{x}^{(q)\mathrm{H}}-\lambda_{\max}(\mathcal{L})\mathbf{I}\right)\mathbf{x}^{(q)}\right]+\tilde{c}\\
&=\lambda_{\max}(\mathcal{L})\left\|\mathbf{x}\right\|_2^2-2\lambda_{\max}(\mathcal{L})\,\mathrm{Re}\left[\mathbf{y}^{\mathrm{H}}\mathbf{x}\right]+\tilde{c},
\end{aligned} \tag{40}$$

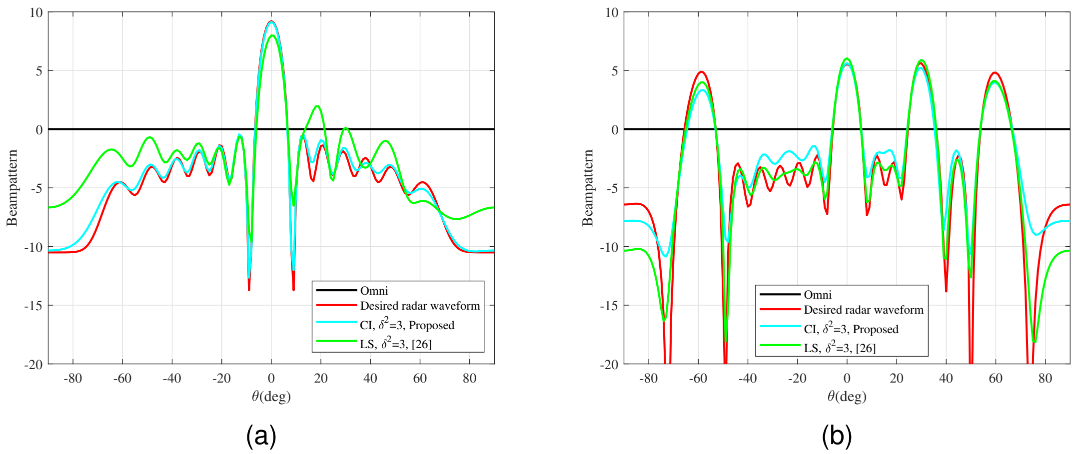

Fig. 12. Radar beampatterns obtained by different waveform design methods. (a) Radar target angles of 0°. (b) Radar target angles of -60°, 0°, 30°, and 60°.

Appendix B

The difficulty of solving problem (29) is from the last constraint. To handel this constraint, we introduce two auxiliary variables, $\mathbf{z} \in \mathbb{C}^{NN_tL}$ and $\mathbf{Z} \in \mathbb{C}^{NN_tL \times NN_tL}$, which are defined as

$$\begin{aligned} \mathbf{z} = [&(\mathbf{F}^{\mathrm{H}} \otimes \mathbf{I}_{N_t})\mathbf{X}_{\mathrm{s}}]_{1,1}, \cdots, (\mathbf{F}^{\mathrm{H}} \otimes \mathbf{I}_{N_t})\mathbf{X}_{\mathrm{s}}]_{1,L}, \cdots, \\ &(\mathbf{F}^{\mathrm{H}} \otimes \mathbf{I}_{N_t})\mathbf{X}_{\mathrm{s}}]_{NN_t,1}, \cdots, (\mathbf{F}^{\mathrm{H}} \otimes \mathbf{I}_{N_t})\mathbf{X}_{\mathrm{s}}]_{NN_t,L}]^{\mathrm{T}}, \quad (41) \\ \mathbf{Z} = \mathbf{z}&\mathbf{z}^{\mathrm{H}}. \end{aligned}$$

Then, the last constraint in (29) can be reformulated as

$$\begin{cases} \beta \mathbf{1}_{NN_tL} \leq \mathrm{diag}(\mathbf{Z}) \leq \beta\chi^2 \mathbf{1}_{NN_tL} \\ \mathbf{Z} = \mathbf{z}\mathbf{z}^{\mathrm{H}} \end{cases} \tag{42}$$

which is equivalent to

$$\begin{cases} \beta \mathbf{1}_{NN_tL} \leq \mathrm{diag}(\mathbf{Z}) \leq \beta\chi^2 \mathbf{1}_{NN_tL} \\ \mathbf{Z} \succeq \mathbf{0} \\ \mathrm{rank}(\mathbf{Z}) = 1. \end{cases} \tag{43}$$

The above constraints can be relaxed by dropping the rank-one constraint, as

$$\begin{cases} \beta \mathbf{1}_{NN_tL} \leq \mathrm{diag}(\mathbf{Z}) \leq \beta\chi^2 \mathbf{1}_{NN_tL} \\ \mathbf{Z} \succeq \mathbf{0}. \end{cases} \tag{44}$$

Therefore, problem (29) is related to be

$$\begin{aligned} \min_{\mathbf{X}_{\mathrm{s}},\beta,\mathbf{Z}} \ & \lambda_{\max}(\mathcal{L}) \left\|\mathrm{vec}(\mathbf{X}_{\mathrm{s}})\right\|_2^2 - 2\lambda_{\max}(\mathcal{L}) \,\mathrm{Re}\left[\mathbf{y}^{\mathrm{H}}\mathrm{vec}(\mathbf{X}_{\mathrm{s}})\right] \\ \text{s.t.} \ & \frac{1}{L}\left\|\left(\mathbf{F}^{\mathrm{H}} \otimes \mathbf{I}_{N_t}\right)\mathbf{X}_{\mathrm{s}}\right\|_{\mathrm{F}}^2 \leq P_{\mathrm{t}} \\ & \left\|\left(\mathbf{F}_{\mathrm{DFT}}^{\mathrm{H}} \otimes \mathbf{I}_{N_t}\right)\mathbf{X}_{\mathrm{s}} - \mathbf{G}_0\right\|_{\mathrm{F}}^2 \leq \delta^2 \\ & \left|\mathrm{Im}\left(\hat{\mathbf{h}}_{k,n}\mathbf{x}_l\right)\right| \leq \left(\mathrm{Re}\left(\hat{\mathbf{h}}_{k,n}\mathbf{x}_l\right) - \Gamma_k\right)\tan\varphi \\ & \beta \mathbf{1}_{NN_tL} \leq \mathrm{diag}(\mathbf{Z}) \leq \beta\chi^2 \mathbf{1}_{NN_tL} \\ & \mathbf{Z} \succeq \mathbf{0}. \end{aligned} \tag{45}$$

Therefore, the optimization problem in (45) is derived by introducing the auxiliary variable $\mathbf{Z}$ and relaxing the rank-one constraint, transforming the original non-convex problem into a SDP.

References

[1] X. Liu, T. Huang, N. Shlezinger, Y. Liu, J. Zhou, and Y. C. Eldar, “Joint Transmit Beamforming for Multiuser MIMO Communications and MIMO Radar,” *IEEE Transactions on Signal Processing*, vol. 68, pp. 3929–3944, 2020.

[2] R. Liu, M. Li, Q. Liu, and A. L. Swindlehurst, “Joint Waveform and Filter Designs for STAP-SLP-Based MIMO-DFRC Systems,” *IEEE Journal on Selected Areas in Communications*, vol. 40, no. 6, pp. 1918–1931, Jun. 2022.

[3] L. Chen, Z. Wang, Y. Du, Y. Chen, and F. R. Yu, “Generalized Transceiver Beamforming for DFRC With MIMO Radar and MU-MIMO Communication,” *IEEE Journal on Selected Areas in Communications*, vol. 40, no. 6, pp. 1795–1808, Jun. 2022.

[4] Z. Cheng, L. Wu, B. Wang, M. R. B. Shankar, and B. Ottersten, “Double-phase-shifter based hybrid beamforming for mmwave dfrc in the presence of extended target and clutters,” *IEEE Transactions on Wireless Communications*, vol. 22, no. 6, pp. 3671–3686, 2023.

[5] D. Ma, N. Shlezinger, T. Huang, Y. Liu, and Y. C. Eldar, “Joint Radar-Communication Strategies for Autonomous Vehicles: Combining Two Key Automotive Technologies,” *IEEE Signal Processing Magazine*, vol. 37, no. 4, pp. 85–97, Jul. 2020.

[6] O. B. Akan and M. Arik, “Internet of Radars: Sensing versus Sending with Joint Radar-Communications,” *IEEE Communications Magazine*, vol. 58, no. 9, pp. 13–19, Sep. 2020.

[7] N. C. Luong, X. Lu, D. T. Hoang, D. Niyato, and D. I. Kim, “Radio Resource Management in Joint Radar and Communication: A Comprehensive Survey,” *IEEE Communications Surveys & Tutorials*, vol. 23, no. 2, pp. 780–814, 2021.

[8] X. Wang, A. Hassanien, and M. G. Amin, “Dual-Function MIMO Radar Communications System Design Via Sparse Array Optimization,” *IEEE Transactions on Aerospace and Electronic Systems*, vol. 55, no. 3, pp. 1213–1226, Jun. 2019.

[9] F. Liu, C. Masouros, A. Li, H. Sun, and L. Hanzo, “MU-MIMO Communications With MIMO Radar: From Co-Existence to Joint Transmission,” *IEEE Transactions on Wireless Communications*, vol. 17, no. 4, pp. 2755–2770, Apr. 2018.

[10] H. Huang, L. Wu, B. Shankar, and A. M. Zoubir, “Sparse array design for dual-function radar-communications system,” *IEEE Communications Letters*, vol. 27, no. 5, pp. 1412–1416, 2023.

[11] T. Huang, X. Xu, Y. Liu, N. Shlezinger, and Y. C. Eldar, “A Dual-Function Radar Communication System Using Index Modulation,” in *2019 IEEE 20th International Workshop on Signal Processing Advances in Wireless Communications (SPAWC)*, Jul. 2019, pp. 1–5, iSSN: 1948-3252.

[12] L. Chen, F. Liu, W. Wang, and C. Masouros, “Joint Radar-Communication Transmission: A Generalized Pareto Optimization Framework,” *IEEE Transactions on Signal Processing*, vol. 69, pp. 2752–2765, 2021.

[13] F. Liu, C. Masouros, A. P. Petropulu, H. Griffiths, and L. Hanzo, “Joint Radar and Communication Design: Applications, State-of-the-Art, and

the Road Ahead," *IEEE Transactions on Communications*, vol. 68, no. 6, pp. 3834–3862, Jun. 2020.

[14] X. Yuan, Z. Feng, J. A. Zhang, W. Ni, R. P. Liu, Z. Wei, and C. Xu, "Spatio-Temporal Power Optimization for MIMO Joint Communication and Radio Sensing Systems With Training Overhead," *IEEE Transactions on Vehicular Technology*, vol. 70, no. 1, pp. 514–528, Jan. 2021.

[15] A. Arora, C. G. Tsinos, M. R. B. Shankar, S. Chatzinotas, and B. Ottersten, "Efficient Algorithms for Constant-Modulus Analog Beamforming," *IEEE Transactions on Signal Processing*, vol. 70, pp. 756–771, 2022.

[16] L. Wu, X. Cheng, H. Huang, D. Ciuonzo, B. Shankar, and B. Ottersten, "Constant-modulus waveform design with polarization-adaptive power allocation in polarimetric radar," *IEEE Transactions on Signal Processing*, vol. 71, pp. 2146–2161, 2023.

[17] W. Zhang, J. Hu, Z. Wei, H. Ma, X. Yu, and H. Li, "Constant modulus waveform design for MIMO radar transmit beampattern with residual network," *Signal Processing*, vol. 177, p. 107735, Dec. 2020.

[18] A. Aubry, A. De Maio, and Y. Huang, "MIMO Radar Beampattern Design Via PSL/ISL Optimization," *IEEE Transactions on Signal Processing*, vol. 64, no. 15, pp. 3955–3967, Aug. 2016.

[19] T. Bouchoucha, S. Ahmed, T. Al-Naffouri, and M.-S. Alouini, "DFT-Based Closed-Form Covariance Matrix and Direct Waveforms Design for MIMO Radar to Achieve Desired Beampatterns," *IEEE Transactions on Signal Processing*, vol. 65, no. 8, pp. 2104–2113, Apr. 2017.

[20] A. Li, D. Spano, J. Krivochiza, S. Domouchtsidis, C. G. Tsinos, C. Masouros, S. Chatzinotas, Y. Li, B. Vucetic, and B. Ottersten, "A Tutorial on Interference Exploitation via Symbol-Level Precoding: Overview, State-of-the-Art and Future Directions," *IEEE Communications Surveys & Tutorials*, vol. 22, no. 2, pp. 796–839, 2020.

[21] A. Li, C. Masouros, A. L. Swindlehurst, and W. Yu, "1-Bit Massive MIMO Transmission: Embracing Interference with Symbol-Level Precoding," *IEEE Communications Magazine*, vol. 59, no. 5, pp. 121–127, May 2021.

[22] T. Tian, G. Li, and T. Zhou, "Power Distribution for an OFDM-Based Dual-Function Radar-Communication Sensor," *IEEE Sensors Letters*, vol. 4, no. 11, pp. 1–4, Nov. 2020.

[23] A. Ahmed, Y. D. Zhang, and Y. Gu, "Dual-function radar-communications using QAM-based sidelobe modulation," *Digital Signal Processing*, vol. 82, pp. 166–174, Nov. 2018.

[24] J. Yang, G. Cui, X. Yu, and L. Kong, "Dual-Use Signal Design for Radar and Communication via Ambiguity Function Sidelobe Control," *IEEE Transactions on Vehicular Technology*, vol. 69, no. 9, pp. 9781–9794, Sep. 2020.

[25] S. Zhou, X. Liang, Y. Yu, and H. Liu, "Joint Radar-Communications Co-Use Waveform Design Using Optimized Phase Perturbation," *IEEE Transactions on Aerospace and Electronic Systems*, vol. 55, no. 3, pp. 1227–1240, Jun. 2019.

[26] F. Liu, L. Zhou, C. Masouros, A. Li, W. Luo, and A. Petropulu, "Toward Dual-functional Radar-Communication Systems: Optimal Waveform Design," *IEEE Transactions on Signal Processing*, vol. 66, no. 16, pp. 4264–4279, Aug. 2018.

[27] S. D. Blunt and E. L. Mokole, "Overview of radar waveform diversity," *IEEE Aerospace and Electronic Systems Magazine*, vol. 31, no. 11, pp. 2–42, Nov. 2016.

[28] H. Griffiths, L. Cohen, S. Watts, E. Mokole, C. Baker, M. Wicks, and S. Blunt, "Radar Spectrum Engineering and Management: Technical and Regulatory Issues," *Proceedings of the IEEE*, vol. 103, no. 1, pp. 85–102, Jan. 2015.

[29] X. Zhang, X. Wang, H. C. So, A. M. Zoubir, and G. Cui, "Min-Max Optimization for MIMO Radar Waveform Design With Improved Power Efficiency," *IEEE Transactions on Signal Processing*, vol. 70, pp. 6112–6127, 2022.

[30] T. Jiang and Y. Wu, "An Overview: Peak-to-Average Power Ratio Reduction Techniques for OFDM Signals," *IEEE Transactions on Broadcasting*, vol. 54, no. 2, pp. 257–268, Jun. 2008.

[31] X. Zhang, X. Wang, and X. Wang, "Joint antenna selection and waveform design for coexistence of MIMO radar and communications," *EURASIP Journal on Advances in Signal Processing*, vol. 2022, no. 1, p. 127, Dec. 2022.

[32] W. Fan, J. Liang, G. Lu, X. Fan, and H. C. So, "Spectrally-Agile Waveform Design for Wideband MIMO Radar Transmit Beampattern Synthesis via Majorization-ADMM," *IEEE Transactions on Signal Processing*, vol. 69, pp. 1563–1578, 2021.

[33] R. Vescovo, "Reconfigurability and Beam Scanning With Phase-Only Control for Antenna Arrays," *IEEE Transactions on Antennas and Propagation*, vol. 56, no. 6, pp. 1555–1565, Jun. 2008.

[34] Y. Huang, S. Hu, S. Ma, Z. Liu, and M. Xiao, "Designing Low-PAPR Waveform for OFDM-Based RadCom Systems," *IEEE Transactions on Wireless Communications*, vol. 21, no. 9, pp. 6979–6993, Sep. 2022.

[35] S. H. Han and J. H. Lee, "An overview of peak-to-average power ratio reduction techniques for multicarrier transmission," *IEEE Wireless Communications*, vol. 12, no. 2, pp. 56–65, Apr. 2005.

[36] X. Hu, C. Masouros, F. Liu, and R. Nissel, "MIMO-OFDM Dual-Functional Radar-Communication Systems: Low-PAPR Waveform Design," *arXiv e-prints*, p. arXiv:2109.13148, Sep. 2021.

[37] X. Hu, C. Masouros, F. Liu, and R. Nissel, "Low-PAPR DFRC MIMO-OFDM Waveform Design for Integrated Sensing and Communications," in *ICC 2022 - IEEE International Conference on Communications*, May 2022, pp. 1599–1604.

[38] C. Masouros and G. Zheng, "Exploiting Known Interference as Green Signal Power for Downlink Beamforming Optimization," *IEEE Transactions on Signal Processing*, vol. 63, no. 14, pp. 3628–3640, Jul. 2015.

[39] Z. Zhang, Q. Chang, F. Liu, and S. Yang, "Dual-Functional Radar-Communication Waveform Design: Interference Reduction Versus Exploitation," *IEEE Communications Letters*, vol. 26, no. 1, pp. 148–152, Jan. 2022.

[40] N. Su, F. Liu, Z. Wei, Y.-F. Liu, and C. Masouros, "Secure Dual-Functional Radar-Communication Transmission: Exploiting Interference for Resilience Against Target Eavesdropping," *IEEE Transactions on Wireless Communications*, vol. 21, no. 9, pp. 7238–7252, Sep. 2022.

[41] J. Song, P. Babu, and D. P. Palomar, "Sequence Design to Minimize the Weighted Integrated and Peak Sidelobe Levels," *IEEE Transactions on Signal Processing*, vol. 64, no. 8, pp. 2051–2064, Apr. 2016.

[42] X. Zhang and X. Wang, "MIMO Radar Waveform Design with Desirable Beampattern and Controllable Power Uniformity," in *2021 International Conference on Control, Automation and Information Sciences (ICCAIS)*, Oct. 2021, pp. 392–397.

[43] J. Song, P. Babu, and D. P. Palomar, "Optimization Methods for Designing Sequences With Low Autocorrelation Sidelobes," *IEEE Transactions on Signal Processing*, vol. 63, no. 15, pp. 3998–4009, Aug. 2015.

[44] M. Grant and B. SP, "CVX: MATLAB software for disciplined convex programming," Jan. 2014.

[45] P. Stoica, H. He, and J. Li, "New Algorithms for Designing Unimodular Sequences With Good Correlation Properties," *IEEE Transactions on Signal Processing*, vol. 57, no. 4, pp. 1415–1425, Apr. 2009.

[46] F. Li, Y. Zhao, and X. Qiao, "A waveform design method for suppressing range sidelobes in desired intervals," *Signal Processing*, vol. 96, pp. 203–211, Mar. 2014.

[47] D. R. Hunter and K. Lange, "A Tutorial on MM Algorithms," *The American Statistician*, vol. 58, no. 1, pp. 30–37, Feb. 2004.

[48] H. He, J. Li, and P. Stoica, *Waveform design for active sensing systems: a computational approach*. Cambridge ; New York: Cambridge University Press, 2012.

[49] D. R. Fuhrmann and G. San Antonio, "Transmit beamforming for MIMO radar systems using signal cross-correlation," *IEEE Transactions on Aerospace and Electronic Systems*, vol. 44, no. 1, pp. 171–186, Jan. 2008.

[50] Y. Sun, P. Babu, and D. Palomar, "Majorization-Minimization Algorithms in Signal Processing, Communications, and Machine Learning," *IEEE Transactions on Signal Processing*, vol. 65, pp. 794–816, Feb. 2017.

Xiang Feng (Member, IEEE) received the graduation degree from the Harbin Institute of Technology, Harbin, China, in 2018. He is currently an Associate Professor with the Harbin Institute of Technology. His research interests include waveform optimization design, new technologies for millimeter wave radar.

Zhongqing Zhao (Student Member, IEEE) received the B.S. degree in Communication Engineering from Yanbian University, China, in 2022. He is currently pursuing the M.S. degree at the School of Information Science and Engineering, Weihai Campus, Harbin Institute of Technology. His research interests include radar-communication integrated waveform design and fusion sensing algorithms.

Huiping Huang (Member, IEEE) is a Marie Curie postdoctoral researcher at Chalmers University of Technology, Gothenburg, Sweden. He received the Ph.D. degree from Darmstadt University of Technology, Darmstadt, Germany, in 2023. He received the B.Eng. and M.Sc. degrees from Shenzhen University, Shenzhen, China, in 2015 and 2018, respectively. He was a recipient of the Chinese Government Award for Outstanding Self-Financed Students Abroad in 2023 and the Marie Curie Postdoctoral Fellowship from the European Union in 2024. He was a technical program committee (TPC) member for several international conferences, including IEEE VTC 2024, and IEEE ICC 2023/2024. His research interests lie in signal processing and wireless communications, with main focuses on direction-of-arrival estimation, source localization, channel estimation, robust adaptive beamforming, sparse array design, compressive sensing, and optimization theory with applications to radar, sonar, navigation, microphone array processing, etc.

Linlong Wu (Senior Member, IEEE) received the B.E. degree in electronic information from Xi'an Jiaotong University (XJTU), Xi'an, China, in 2014, and the Ph.D. degree in electronic and computer engineering from The Hong Kong University of Science and Technology (HKUST), Hong Kong, in 2018. He was a Research Engineer with the Wireless Network Group, Alibaba Cloud, from November 2018 to October 2020, working on designing and building commercial RFID-based localization systems. Since November 2020, he has been with the Interdisciplinary Centre for Security, Reliability and Trust (SnT), University of Luxembourg, and is currently a Research Associate with the Signal Processing Applications in Radar and Communications (SPARC) Group. His research interests include signal processing, optimization and machine learning with applications in waveform design, integrated sensing and communication, and the IoT networks.

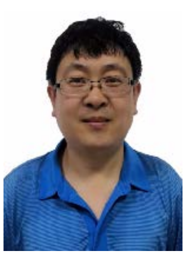

Zhanfeng Zhao (Member, IEEE) received the graduation degree from the Harbin Institute of Technology , Harbin, China, in 2010. He is currently a Professor with the Harbin Institute of Technology. His research interests include laser communication, radar signal processing, and sensor technology.